Facile fabrication of acidified g-C$_3$N$_4$/g-C$_3$N$_4$ hybrids with enhanced photocatalysis performance under visible light irradiation

Xiaolong Yang [a,1], Fangfang Qian [a,1], Guojun Zou [b], Mengli Li [c], Jinren Lu [a], Yiming Li [a], Mutai Bao [a,*]

[a] Key Laboratory of Marine Chemistry Theory and Technology, Ministry of Education, Ocean University of China, 238 Song-Ling Road, Qingdao 266100, PR China
[b] State Key Laboratory for Oxo Synthesis and Selective Oxidation, Lanzhou Institute of Chemical Physics, Chinese Academy of Sciences, 18 Tian-Shui Road, Lanzhou 730000, PR China
[c] State Key Laboratory of High Performance Ceramics and Superfine Microstructure, Shanghai Institute of Ceramics, Chinese Academy of Sciences, 1295 Ding-Xi Road, Shanghai 200050, PR China

ARTICLE INFO

ABSTRACT

A highly efficient visible-light-driven acidified g-C$_3$N$_4$ (ACNS)/g-C$_3$N$_4$ isotype heterojunction photocatalysts were synthesized by ultrasonic dispersion assisted electrostatic self-assembly strategy for the first time. The photocatalytic oxidation ability of the novel photocatalysts were evaluated using methyl orange (MO) as a target pollutant. The obtained ACNS/g-C$_3$N$_4$ photocatalysts were characterized by X-ray powder diffraction (XRD), Fourier transform infrared spectrometry (FTIR), UV–vis diffuse reflection spectroscopy (DRS), Scanning electron microscopy (SEM), Transmission electron microscopy (TEM) and X-ray photoelectron spectroscopy (XPS) methods. The photocatalysts exhibited a significantly enhanced photocatalytic performance in degrading MO under visible light illumination ($\lambda > 420$ nm) compared with the pristine ACNS and g-C$_3$N$_4$ solely. The optimal ACNS content for the photocatalytic activity of the heterostructured composites was determined. The 30 wt.% ACNS/g-C$_3$N$_4$ exhibited the highest photocatalytic activity, which showed a reaction rate constant as high as 0.0216 min^{-1}, 4.3 times higher than that of bare g-C$_3$N$_4$. The mechanism of the photocatalysts was investigated by determination of reactive species in the photocatalytic reactions and photoluminescence technique. The quenching effects of different scavengers displayed that the reactive h$^+$ and $\cdot$O$_2^-$ played major role in the reaction systems. The synergic effect between the ACNS and g-C$_3$N$_4$ was found to lead to an improved photo-generated carrier separation and hence the photocatalytic activities of the composite photocatalysts were increased significantly.

© 2016 Published by Elsevier B.V.

1. Introduction

In recent years, energy shortages and environmental pollution have become the focus of world attention. As one of the most promising solutions for these problems, semiconductor photocatalysis has attracted intensive interests from the viewpoint of utilizing solar light, as it provides a green and potential route for the wide applications in clean energy production, environmental remediation, and final chemical synthesis [1]. Of the well-known semiconductor photocatalysts, TiO$_2$ has been proved to be the most representative and extensively used material owing to its chemi-

cal and physical inertness, nontoxicity, and low-cost [2]. However, its inherent drawbacks in photocatalysis are the low solar energy utilization efficiency because of its wide band gap (3.20 eV) and rapid recombination of photoinduced electron-hole carriers, which largely limit its applications [3–5].

Recently, an organic and metal-free polymeric photocatalyst, polymeric graphitic carbon nitride (g-C$_3$N$_4$) with a proper band gap (2.7 eV) has attracted tremendous attention both in photocatalytic H$_2$ production and photocatalytic degradation of contaminants under visible light irradiation [6]. In general, g-C$_3$N$_4$ has been considered as a "sustainable" advanced photocatalyst possessing several advantages such as visible light photocatalytic response, inexpensive, nontoxicity and stable in solutions with pH 0–14 [6–9]. Therefore, g-C$_3$N$_4$ is believed to be an important visible-light photocatalyst for practical application in large scale, and has drawn
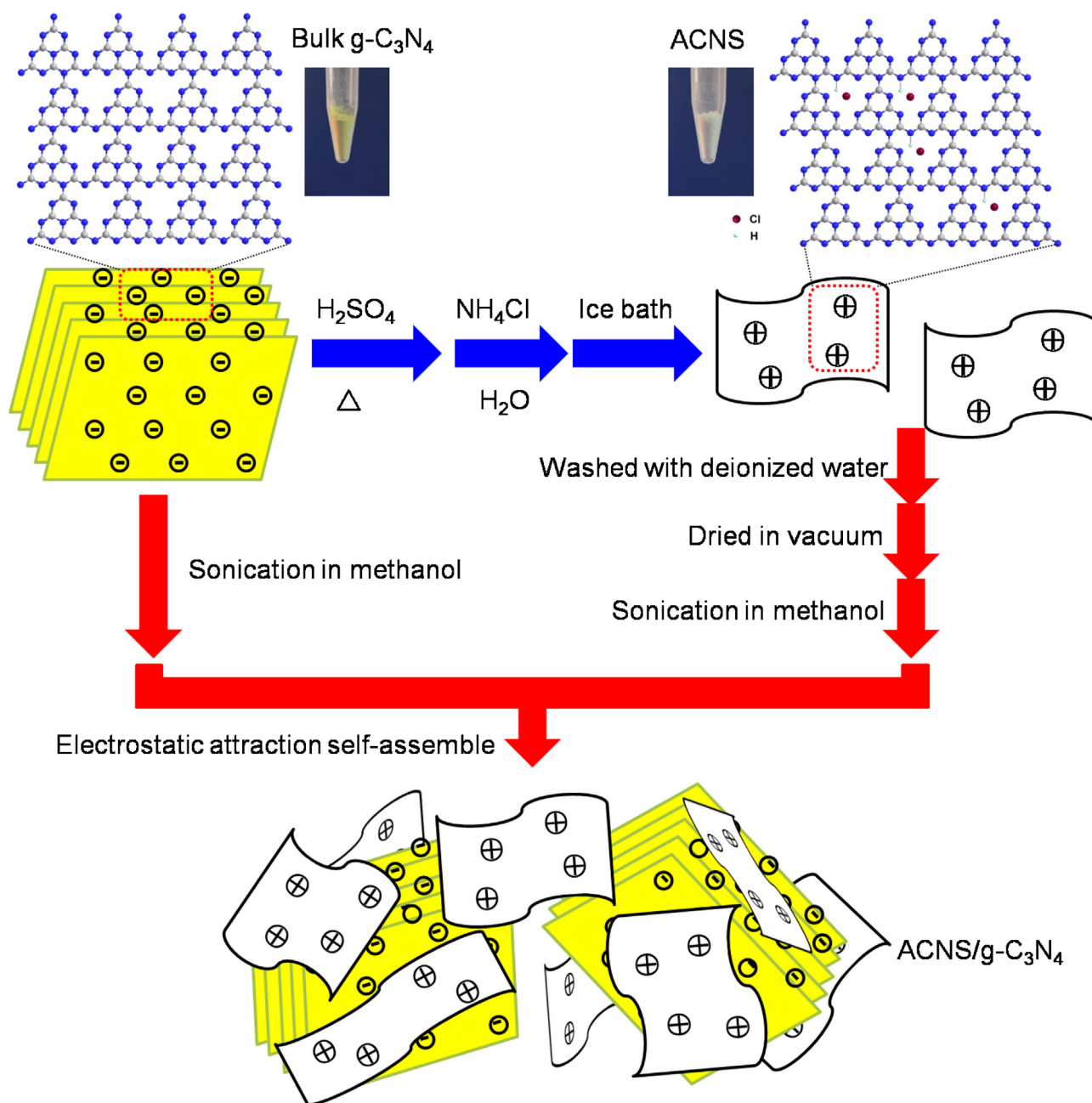
Fig. 1. Schematic diagram for the synthesis process of ACNS/g-C$_3$N$_4$ samples *via* a combined ultrasonic dispersion and electrostatic self-assembly strategy.

intense attention for many researchers [7–10]. Nevertheless, the efficiency of pristine g-C$_3$N$_4$ is still limited due to its high recombination rate of photo-generated electron-hole pairs [11–14].

To date, extensive efforts have been exploited to enhance the photocatalytic activity of g-C$_3$N$_4$ by adjusting the band gap with heteroatoms-doping, changing morphology and construction of heterostructure, *etc.*, which are able to promote the separation of photogenerated electrons and holes [12,14–16]. In principle, formation of heterostructure demonstrates a great potential to promote the photocatalytic performance of g-C$_3$N$_4$ among these approaches because the electron-hole pairs can be efficiently separated at the interface of two semiconductors, and charge carriers could transfer across the interface of the heterostructure to restrain the recombination [17–19]. Besides allotypic g-C$_3$N$_4$-based heterojunction including g-C$_3$N$_4$/graphene [20], TiO$_2$/g-C$_3$N$_4$ [21,22], MoS$_2$/g-C$_3$N$_4$ [20], Bi$_2$WO$_6$/g-C$_3$N$_4$ [23] and BiOBr/g-C$_3$N$_4$ [24,25],

the strategy was further advanced by constructing isotype heterojunctions, such as sulfur-mediated g-C$_3$N$_4$/g-C$_3$N$_4$ [17], as well as g-C$_3$N$_4$ (thermo polymerization of urea)/g-C$_3$N$_4$ (thermo polymerization of thiourea) [26]. The differences in the band structure between two different phases enable the formation of isotype nanojunctions at the interface of different components, leading to the enhanced photocatalytic activity arising from promoted charge separation. Hence, the construction of heterojunction between g-C$_3$N$_4$ and functionalized g-C$_3$N$_4$ is a recommended choice to promote the separation of electron-hole pairs across the interface for enhanced photocatalytic activity.

In recent years, protonation of g-C$_3$N$_4$ have attracted extensive attention because it not only provides better dispersion and a high surface area but also enables the adjustment of electronic band gaps and higher ionic conductivity for pristine g-C$_3$N$_4$ [27,28]. However, few reports focus on the construction of protonated
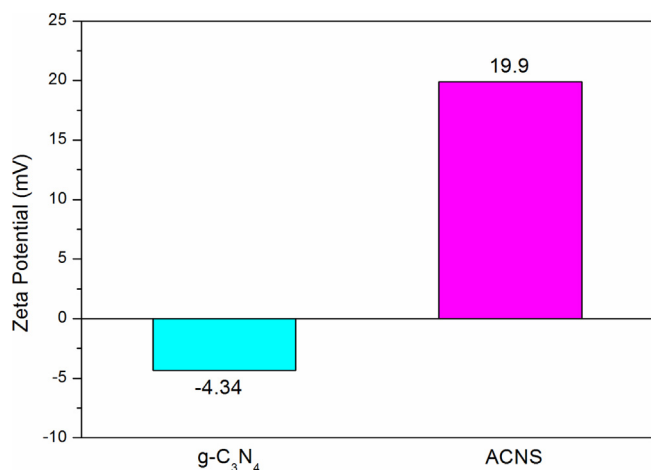
Fig. 2. Zeta potential of the g-C_3N_4 and ACNS dispersed in deionized water (The pH for g-C_3N_4 and ACNS suspension is 6.77 and 6.46, respectively).

Fig. 3. XRD patterns of g-C_3N_4, ACNS/g-C_3N_4 and ACNS samples.

g-C_3N_4/pristine g-C_3N_4 heterojunction. Taking into account that we have synthesized acidified g-C_3N_4 (due to the more profound protonation, we tend to call it acidified instead of protonated g-C_3N_4 here) in our previous work, which exhibits the characteristics of a poly-ammonium salt, showing a larger band gap and the changed photophysical behavior of photoexcited charge carriers [29]. Hence, coupling the acidified g-C_3N_4 (ACNS) and intrinsic g-C_3N_4 to construct well-matched ACNS/g-C_3N_4 isotype heterojunction may provide an alternative novel pathway to address the intrinsic drawbacks of g-C_3N_4 for photochemical applications. To the best of our knowledge, there are no reports to study coupling ACNS with g-C_3N_4 to construct heterojunction photocatalyst.

Herein, a novel ACNS/g-C_3N_4 isotype photocatalysts were firstly synthesized by the electrostatic attraction of oppositely charged materials to form the hybrid nanostructures at ambient temperature. The ACNS/g-C_3N_4 heterostructured photocatalysts exhibited enhanced photocatalytic activity for degradation of MO under visible light irradiation over g-C_3N_4 alone. The separation mechanism of photogenerated electrons and holes of the photocatalysts was investigated by determination of reactive species in the photocatalytic reactions and photoluminescence technique. The enhanced photocatalytic performance can be ascribed to the efficient charge separation and transfer across the heterojunction interface. The present work demonstrated that rational design and construction of isotype heterojunction related with protonated g-C_3N_4 was an effective strategy for the development of efficient visible-light photocatalysts.

2. Experimental

2.1. Chemicals and materials

Melamine (99.0%), NH_4Cl (99.5%), Concentrated sulfuric acid (98%, H_2SO_4) and Oleum (with free SO_3 20∼25%) were obtained from Sinopharm Chemical Reagent Co., Ltd. (PR China). TiO_2 (P25, 20% rutile and 80% anatase) was obtained from Degussa (Germany). Deionized water was used during the experimental process, prepared using an ultra-pure purification system. All the chemicals were of analytically pure grade and used without further purification.

2.2. Preparation of bulk g-C_3N_4

Bulk g-C_3N_4 sample was synthesized by directly heating melamine in a semi-closed system according to a previously
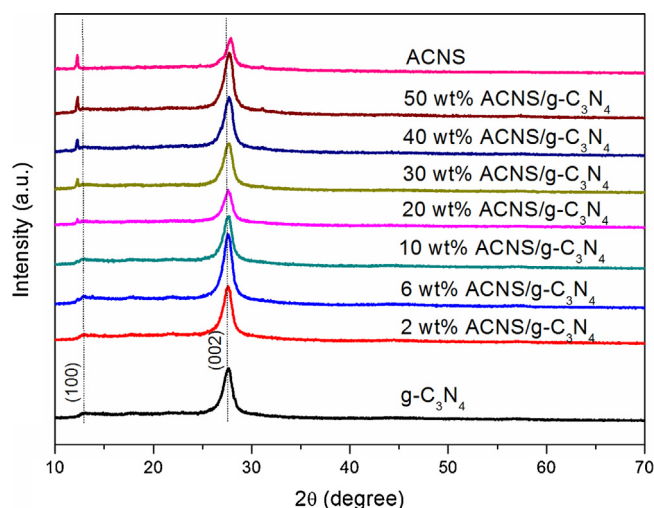
reported procedure [30]. In a typical synthesis, 10 g of melamine was put into an alumina crucible which was heated in a muffle furnace from room temperature to 600 °C with a heating rate of 2.3 °C min^{-1}. After calcination at 600 °C for 4 h, the alumina crucible was cooled naturally to room temperature. The as-prepared g-C_3N_4 was collected and ground into powder for further use.

2.3. Preparation of ACNS

ACNS was synthesized according to a previously reported procedure [29]. In brief, 4.0 g of yellow bulk g-C_3N_4, 52 g H_2SO_4 (98%), and 20 g oleum (with free SO_3 20∼25%) were added into a 100 mL flask successively and stirred for 3 h. The obtained transparent yellow solution was natural cooled and then injected into 800 mL of deionized water. An appropriate of NH_4Cl was added into the solution afterward and the solution was maintained stirring at 70 °C for 2 h, and then hot filtered to remove residues. The obtained clear and colorless filtrate was placed in an ice bath. Pure white precipitation generated and was collected by filter, washed with deionized water, and dried at 60 °C in vacuum. The obtained pure white fine powder was ACNS.

2.4. Construction of ACNS/g-C_3N_4 heterojunction

The typical construction of ACNS/g-C_3N_4 photocatalysts was as follows: An appropriate amount of ACNS and g-C_3N_4 powder were completely dispersed in methanol assisted by ultrasonication for 4 h. The as prepared ACNS and g-C_3N_4 suspended solution were mixed together and stirred vigorously in a fume hood for 6 h. After volatilization of the methanol, an opaque powder was obtained after drying at 50 °C overnight. In this way, a series of ACNS (wt.%)/g-C_3N_4 photocatalysts (wt. = 0, 2.0, 6.0, 10.0, 20.0, 30.0, 40.0, 50.0, 100.0) were synthesized.

2.5. Photoreaction apparatus and procedure

The photocatalytic activities of obtained samples were evaluated by degrading methyl orange (MO) in aqueous solution under visible light illumination ($\lambda > 420$ nm). The photocatalytic degradation of MO was carried out in 100 mL of Pyrex double-jacket reactor. The distance between the light source and the surface of the reaction solution was 10 cm. A water bath connected with a pump was used to maintain the reaction temperature at 25 ± 2 °C, and a magnetic stirrer was used to keep the photocatalyst dispersed homogeneously in the reaction solutions. A 300 W Xe lamp (Perfect
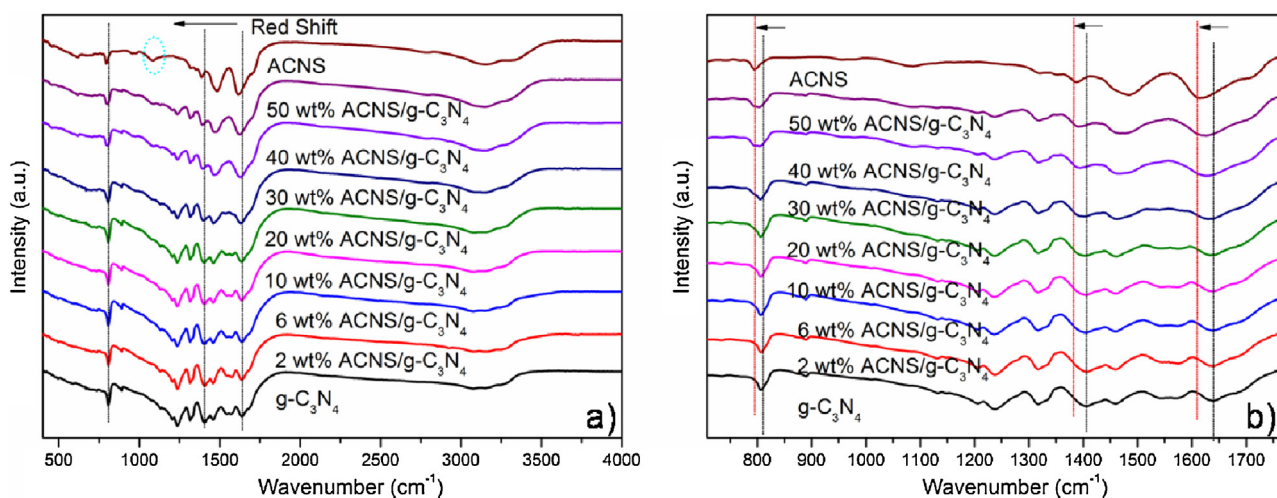
Fig. 4. FTIR spectra of (a) g-C_3N_4, ACNS/g-C_3N_4 and ACNS samples. (b) Enlarged FTIR spectra from (a).

Light, PLS-SXE300) equipped with a 420 nm cut-off filter provided visible-light irradiation. In a typical run, 50 mg of photocatalyst was dispersed into 50 mL MO aqueous solution with a concentration of 10 mg L^{-1}. Prior to irradiation, the suspension was magnetically stirred in the dark for 30 min to ensure the establishment of an adsorption-desorption equilibrium. Then, at selected time intervals, 4 mL of samples was collected and centrifuged at 12,000 rpm for 15 min to remove the photocatalyst particles from the solution. After that, the resulting supernatant was analyzed using a UV–vis light spectrophotometer (Lambda20, PerkinElmer, USA) and the characteristic absorption peak of MO at 476 nm was used to determine the extent of its decomposition. A blank test was also carried out on an aqueous MO solution without photocatalyst under the same condition. In order to determine the reproducibility of the results, at least duplicated runs were carried out for each condition for averaging the results. In addition, the recyclability of the catalyst was also studied by washing and drying the catalyst before the next cycle.

2.6. Structural characterization methods

Zeta potential measurements were obtained by dynamic light-scattering analysis using the Zetasizer Nano ZS (Malvern Instruments). In brief, 20 mg of the sample was dispersed in 50 mL of deionized water by sonication at room temperature. The crystalline structure of the g-C_3N_4, ACNS, and various ACNS/g-C_3N_4 photocatalysts were analyzed by X-ray powder diffraction (XRD) (X′pert, PANalytical, Dutch) using Cu Kα radiation (λ = 1.54050 Å). Crystallite size of the catalysts was calculated by the Scherrer equation. The molecular structural information was determined from a fourier transform infrared spectroscopy (FTIR) (NEXUS 870) by the KBr pellet method in the range of 400–4000 cm^{-1}. The surface morphology of the as-developed samples was examined by field emission scanning electron microscopy (FESEM) (JEOL JSM-6701F) and transmission electron microscope (TEM) (JEM-2010) with an accelerating voltage of 200 kV. Room-temperature UV–vis diffuse reflectance spectroscopy (UV–vis DRS) was recorded on a Shimadzu UV-2550 UV–vis spectrophotometer and BaSO$_4$ as the reference material. Absorption spectra were calculated from the reflectance data with the Kubelka-Munk function. X-ray photoelectron spectra (XPS) were taken on a photoelectron spectrometer (VG ESCALAB 210) with a monochromatic X-ray source of Mg Kα (hν = 1253.6 eV), calibrated internally by carbon deposit C (1s) binding energy (BE) at 284.8 eV. The photoluminescence (PL) measurements were recorded on a fluorescence spectrometer (PerkinElmer, LS55) at

room temperature. The samples were excited at a wavelength of 330 nm with a scanning speed of 600 nm min^{-1}. The widths of excitation slit and emission slit were fixed at 10 nm. Total organic carbon (TOC) of the MO solutions was recorded by TOC/TNb Analyzer (Multi N/C 3100, Analytikjena, Germany). The filtered sample solutions were analyzed by ESI/MS in the negative ion modes on mass spectrometer (Bruker maXis UHR-TOF). ESI/MS conditions were: scan range, m/z 50–500; heat block temperature, 180 °C; interface voltage, 4.5 kV; CDL voltage, 20 V. The solutions (10 μL) were injected into the LC/MS system, and the flow rate of the mobile phase acetonitrile-ammonium acetate 1 mM pH 6.8 (24/76 (v/v)) was 0.20 mL min^{-1}.

2.7. Photoelectrode preparation and photoelectrochemical measurements

An FTO glass (13 × 10 mm) was first ultrasonically cleaned with acetone of analytical grade for 5 min, rinsed with deionized water, and then dried with a clean, dry air flow. One longitudinal edge of the conductive side was then carefully covered with insulating tape, with the exposed effective area of the FTO glass measuring 1 cm^2. In total, 0.01 g of the prepared powder was mixed with 0.1 mL of deionized water in an agate mortar, and the mixture was carefully ground for 10 min to form a homogeneous suspension. Then, 0.025 mL of the as-prepared suspension was evenly distributed onto the exposed area of the conductive side of the FTO glass. The insulating tape on the edge of the FTO glass was removed after the suspension dried in the air. Finally, the FTO glass deposited with the as-prepared suspension was heated to 120 °C for 2 h under vacuum condition. A copper wire was connected to the conductive side of the FTO glass using conductive silver tape. The uncoated parts of the conductive side of the FTO glass were isolated with parafilm after the conductive silver tape had dried.

Photoelectrochemical measurements were performed in a three-electrode experimental system using Electrochemical Workstation (Autolab PGSTAT302N electrochemical workstation). The prepared photoelectrode, Ag/AgCl (saturated KCl) electrode, and Pt electrode acted as the working, reference, and counter electrodes, respectively. The electrolyte was 0.1 mol L^{-1} Na$_2$SO$_4$. Electrochemical impedance spectroscopy (EIS) tests were performed at open circuit potential over the frequency range between 100 kHz and 50 mHz, with an AC voltage magnitude of 5 mV, using 12 points/decade. Mott–Schottky plots were measured at ambient temperature under dark condition. The potential range is −2.0 to
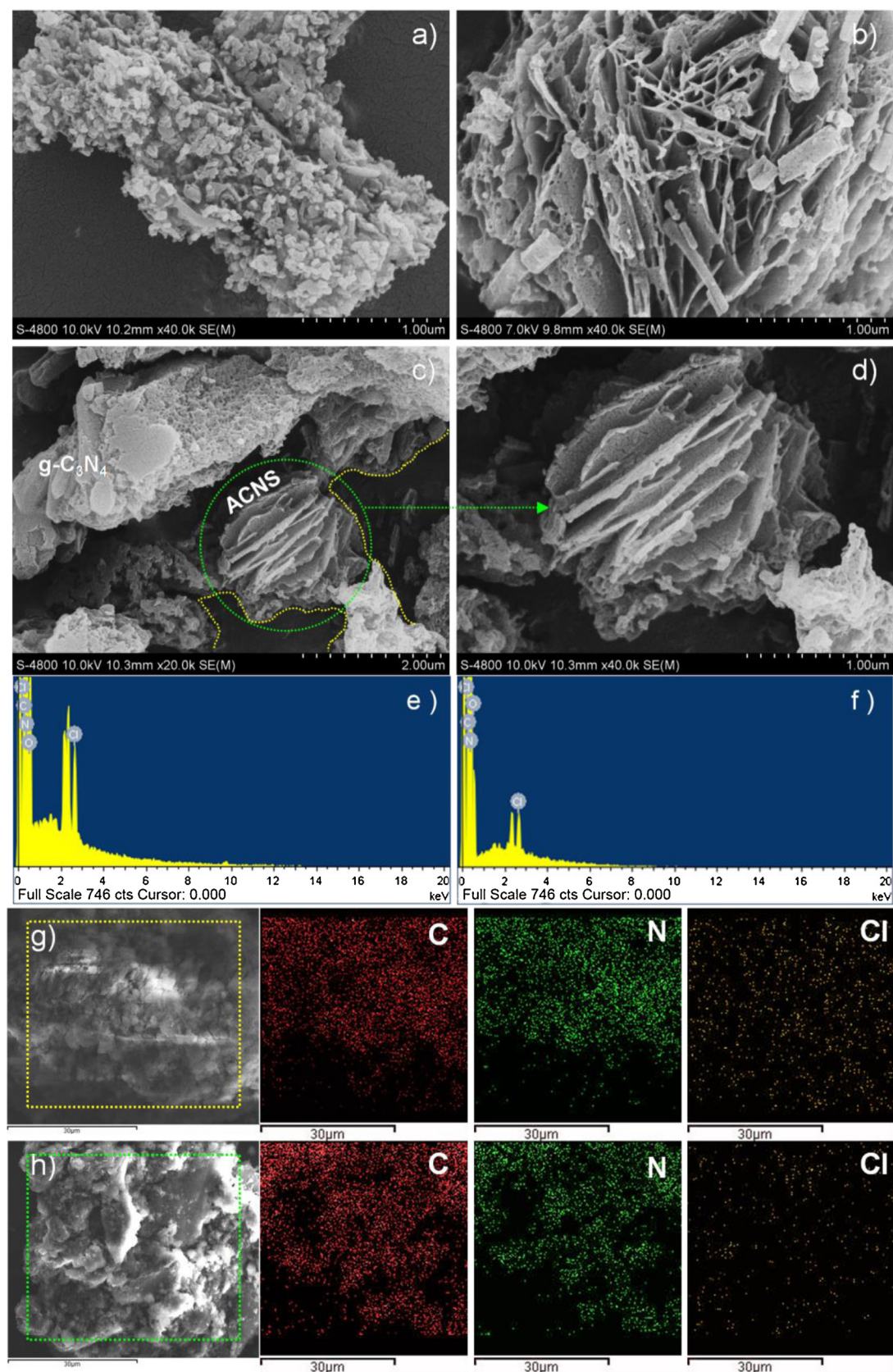
Fig. 5. FESEM images of (a) g-C$_3$N$_4$; (b) ACNS and (c, d) 30 wt.% ACNS/g-C$_3$N$_4$; the area marked in (c) is magnified in (d). EDS spectra and corresponding elemental mapping of (e, g) ACNS and (f, h) 30 wt.% ACNS/g-C$_3$N$_4$.

1.0 V and the frequency is 1000 Hz with an AC voltage magnitude of 10 mV and a scan rate of 10 mV s^{-1}.

3. Results and discussion

3.1. Synthesis approach

The ACNS/g-C$_3$N$_4$ composites were fabricated *via* a facile and effective ultrasonication-assisted electrostatic self-assembly strategy, which is a simple, versatile and significantly inexpensive approach to produce nanoscale heterogeneous semiconductor photocatalysts compared to the methods of electrodeposition, calcination and hydrothermal, *etc.* The components of oppositely charged species can be easily assembled in such an electrostatic self-assembly process [31], as pictorially shown in Fig. 1. The acidified procedure resulted in the surface charge modification from a negatively charged surface to a positively charged surface. Evidently, the zeta potential value of ACNS was measured to be +19.9 mV when dispersed in deionized water as compared to that of −4.34 mV for pristine g-C$_3$N$_4$ (Fig. 2). Therefore, it was clear that the spontaneous self-assembly between the positively charged ACNS and the negatively charged g-C$_3$N$_4$ was realized by the electrostatic interactions to construct the ACNS/g-C$_3$N$_4$ hetrostructure.

3.2. Characterization of the ACNS/g-C$_3$N$_4$ photocatalysts

The XRD patterns of pristine g-C$_3$N$_4$, ACNS and ACNS/g-C$_3$N$_4$ photocatalysts are presented in Fig. 3. Two peaks are observed in the XRD patterns for g-C$_3$N$_4$. It is clear that g-C$_3$N$_4$ shows two basic diffraction peaks at around 12.8° and 27.6° (JCPDS 087-1526), the peak observed at 12.8° indexed as the (100) plane corresponds to the in-plane structural packing motif of aromatic segments. This calculated distance is 0.689 nm corresponding to the hole-to-hole distance in the nitride pores. Another intense peak around 27.6° corresponds to the interlayer stacking of aromatic units of CN with an interlayer distance of 0.323 nm, ascribing to the (002) plane of the stacking of the conjugated aromatic system. The two diffraction peaks are in good agreement with the reported results of g-C$_3$N$_4$ [26,32]. In addition, these two typical diffraction peaks of g-C$_3$N$_4$ are still present in the ACNS after acidified pretreatment, highlighting that the crystal structures of g-C$_3$N$_4$ are well-maintained. Some minor changes are also observed with respect to ACNS, the (100) peak of ACNS becomes pronounced and shifts to a lower angle of 12.25°, indicating the increase of plane size and the increasingly stretched properties of ACNS. Further, the (002) peak of ACNS shifts to a higher angle of 27.84°, which gives an interplanar distance of d = 0.320 nm, demonstrating tighter packing aggregates in the ACNS nanosheets, as described earlier, the single layers of g-C$_3$N$_4$ are potentially undulated, acidification process would cause undulating single layers in g-C$_3$N$_4$ to be planarized by pushing bridge nitrogen atom of N—(C)$_3$ group to move to the tri-s-triazine plane, thus leading to more flattened layers and narrower layer spacing in the acidified g-C$_3$N$_4$ [29,33]. For the ACNS/g-C$_3$N$_4$ composites, it can be found that the intensities of diffraction peaks of (100) become stronger with the increase in the contents of ACNS gradually. When the amount of ACNS is lower than 20 wt.%, the characteristic peaks (100) of ACNS cannot be found. Nevertheless, pronounced diffraction peaks corresponding to ACNS (12.25) appeared when the ACNS content increased from 20 wt.% to 50 wt.%. It is suggested that ACNS may be highly dispersed on the surface of g-C$_3$N$_4$.

The chemical structure of pristine g-C$_3$N$_4$, ACNS and ACNS/g-C$_3$N$_4$ composites photocatalysts are analyzed by FTIR and the results are shown in Fig. 4 . For g-C$_3$N$_4$, the broad peak ranging from 3000 to 3500 cm^{-1} are attributed to the N—H band

and O—H stretches due to the free amino groups and adsorbed hydroxyl species, respectively [10,11,34]. The strong bands at the 1200–1650 cm^{-1} region are found in the spectrum, the absorption band at 1640 cm^{-1} is attributed to C—N stretching, while the three at 1555 cm^{-1}, 1461 cm^{-1} and 1405 cm^{-1} are contributed to the typical stretching vibration modes of C—N heterocycles [11,16,24,25]. The bands at 1319 cm^{-1} and 1243 cm^{-1} correspond to stretching vibration of connected units of C—NH—C, which is also supported by the broad weak band at 3000∼3500 cm^{-1} for hydrogen-bonding interactions mentioned above [16,29,35]. In addition, The intense band at 810 cm^{-1} represents the characteristic breathing mode of tri-s-triazine rings units [26]. In the case of ACNS, the typical peak of the breathing mode of the triazine units at 795 cm^{-1} is still reserved. The absorption peaks at about 1318 and 1240 cm^{-1} become less pronounced because of electrostatic attraction between proton charge and N—(C)$_3$ groups [29]. Due to minor hydrolysis of g-C$_3$N$_4$, weak absorption peak at 1085 cm^{-1} corresponding to the stretching vibration of C—O appears, which is consistent with the reported IR results of protonated g-C$_3$N$_4$ or exfoliated nanosheets [27,36]. With respect to ACNS/g-C$_3$N$_4$ composites, it can be found that the intensities of peak at 1318 and 1420 cm^{-1} of g-C$_3$N$_4$ become less pronounced with the increase in the contents of ACNS gradually. Notably, with increased ACNS amounts in the samples, the band at 1640 cm^{-1} attributed to C—N stretching and 1405 cm^{-1} attributed to typical stretching vibration modes of C—N heterocycles slightly red shifts to a lower wavenumber in the ACNS/g-C$_3$N$_4$ hybrid as shown in Fig. 4b for detail, the same phenomenon is also observed in terms of breathing mode of tri-s-triazine rings at 795 cm^{-1}, which suggests an interaction between tri-s-triazine units of ACNS and that of g-C$_3$N$_4$ is formed by electrostatic self-assembly approach.

The morphology and microstructure of the g-C$_3$N$_4$, ACNS and ACNS/g-C$_3$N$_4$ samples are revealed by FESEM and TEM. As depicted in Figs. 5 a and 6 a, bulk g-C$_3$N$_4$ are composed of a large number of aggregated morphology with a large size and lamellar structure, which is the typical structure characteristic of g-C$_3$N$_4$ synthesized by the polymerization method [15,27,35,36]. Compared with g-C$_3$N$_4$, the representative morphology of ACNS appear as orderly agglomerates, which is consisted of a great deal of ultra-thin sheet-like ACNS [29] (Figs. 5 b and 6 b). 2D nanosheets are extremely advantageous for promoting photocatalysis efficiency in terms of providing abundant reactive sites and short bulk diffusion length for reducing the recombination probability of photoexcited charge carriers [18,29]. By employing this green electrostatic self-assembly route, we have incorporated the 2D structures of ACNS with g-C$_3$N$_4$. The 30 wt.% ACNS/g-C$_3$N$_4$ combine the characteristic of the g-C$_3$N$_4$ and ACNS mentioned above, forming a more compact and well-dispersed structure as shown in Figs. 5 c, d and 6 c, d. Fig. 5d is the magnified image obtained from the round area marked in Fig. 5c, which shows that typical structure characteristic of ACNS with sheet-like morphology. The good interfacial contact between g-C$_3$N$_4$ and ACNS is favorable for charge transfer between the two components. The presence of elements C, N, and Cl in the ACNS and ACNS/g-C$_3$N$_4$ composites is observed in Energy dispersive X-ray spectroscopy (EDS) spectra in Fig. 5e, f. Elemental mapping images further verify the uniform distribution of Cl throughout ACNS/g-C$_3$N$_4$ at the nanoscale as shown in Fig. 5h, which demonstrates that ACNS are well dispersed on the surface of g-C$_3$N$_4$. It is beneficial for the strong interaction between ACNS and g-C$_3$N$_4$, being consistent well with the results from the FTIR results.

The optical adsorption of g-C$_3$N$_4$, ACNS and ACNS/g-C$_3$N$_4$ with different ACNS mass ratios are measured using UV–vis diffuse reflectance spectroscopy (Fig. 7). It is known that the optical absorption of a semiconductor is closely related to its electronic structure. It is clear that from Fig. 7a, the g-C$_3$N$_4$ shows absorption wavelengths from the UV to the visible range, which can be assigned to
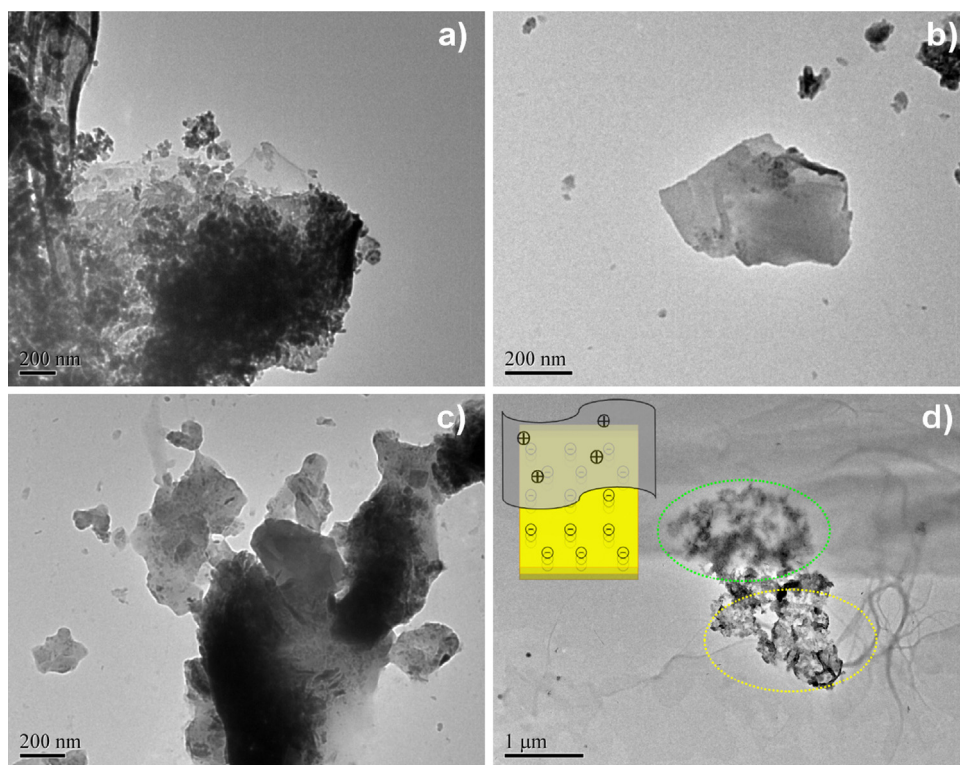
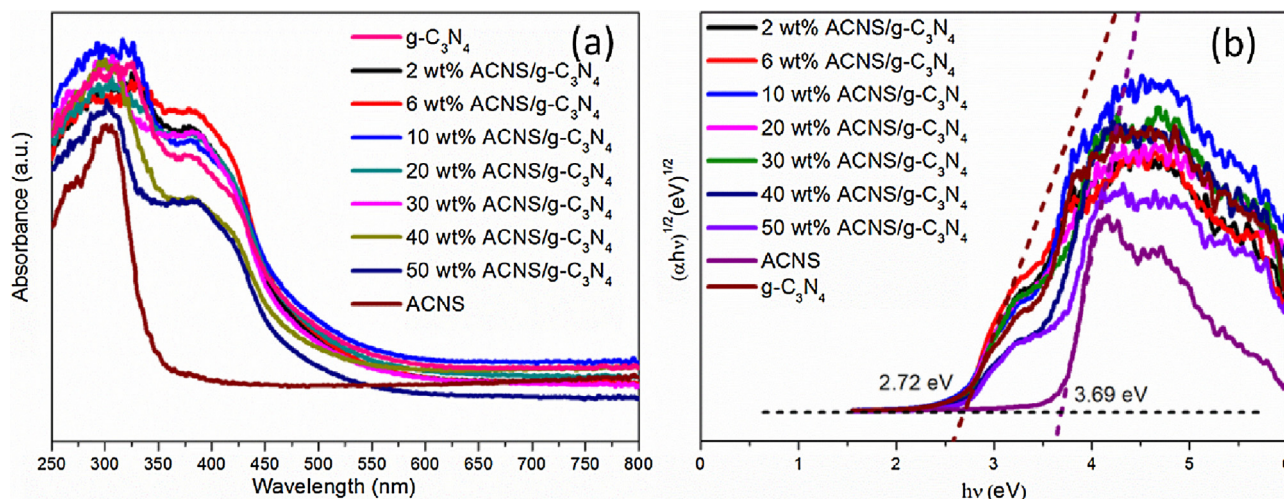**Fig. 6.** TEM images of (a) g-C_3N_4, (b) ACNS and (c, d) 30 wt.% ACNS/g-C_3N_4.

Fig. 7. (a) UV–vis diffuse reflectance spectra of the photocatalysts and (b) their corresponding band gap plots.

the intrinsic band gap of g-C_3N_4 [37]. Compared with pristine g-C_3N_4, the absorption edge of ACNS (348 nm) shows a remarkable blue shift with respect to the bulk sample and the derived band gap of the light absorbed is 3.69 eV as shown in Fig. 7b.

The larger band gap of ACNS can be presumably ascribed to two factors. Specifically, quantum confinement effect arises when the ultrathin thickness of the synthesized g-C_3N_4 nanosheets approaches that of de Broglie wavelength, which limits the electron motion in this dimension, and causes the splitting of energy levels [27,28,38,39]. This seems to be similar with the results of titania nanosheet and anatase, the band gap energy of the titania nanosheet and the anatase is 3.8 and 3.2 eV, respectively [40]. In addition, the salification of the heterocyclic nitrogen atom brings more positive charges to the tri-s-triazine unit, which will attract

the lone electron pair of the bridge nitrogen atom and reduce its repulsion with the C—N bond. This would push bridge nitrogen atom to move to the tri-s-triazine plane and reduce the electron density of the single layers of g-C_3N_4, resulting in a larger optical bandgap in ACNS [29].

Furthermore, the ACNS/g-C_3N_4 samples present the hybrid absorption features of ACNS and g-C_3N_4, the absorption edges of ACNS become more evident with the increase of ACNS content in the heterostructured samples. On the one hand, when the amounts of ACNS are below 30 wt.%, the absorption spectra are identical as the g-C_3N_4. On the other hand, when the content of ACNS was above 30 wt.%, decreased light adsorption intensity in the region of visible light ranging from 400 to 550 nm is observed in comparison to the pristine g-C_3N_4. The band gap energies of semiconductors can be
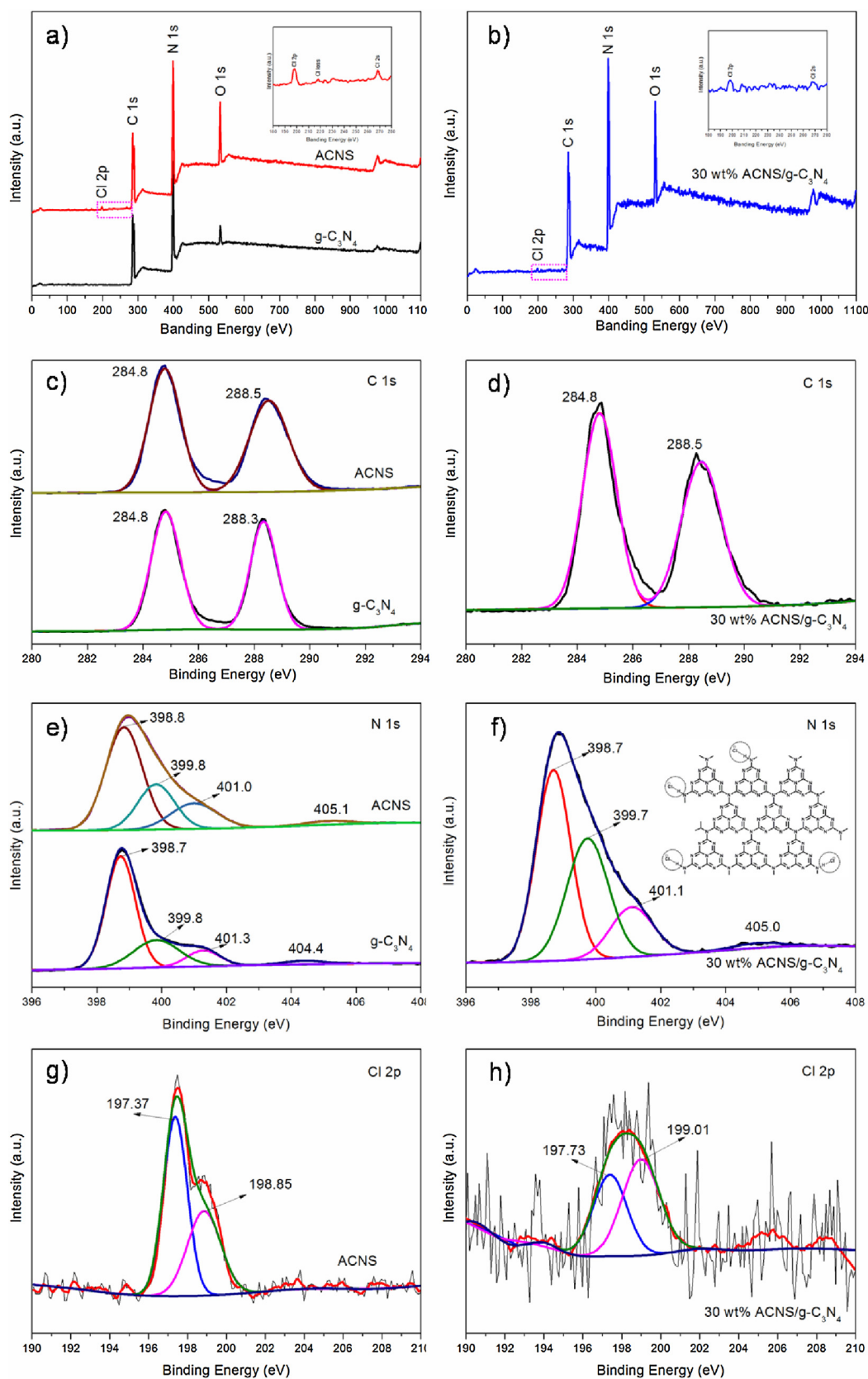
Fig. 8. XPS spectra of g-C_3N_4, ACNS and 30 wt.% ACNS/g-C_3N_4. (a, b) survey; (c, d) C 1s; (e, f) N 1s; (g, h) Cl 2p.

estimated by Kubelka−Munk transformation, $\alpha h\upsilon = A(h\upsilon - E_g)^{n/2}$, where α represents the absorption coefficient, υ is the light frequency, E_g is the band gap energy, A is a constant and n depends on

the characteristics of the transition in a semiconductor. For g-C_3N_4, the value of n is 4 for the indirect transition [34,41]. Thus, the band gap energy (E_g) estimated from the intercept of the tangents to the

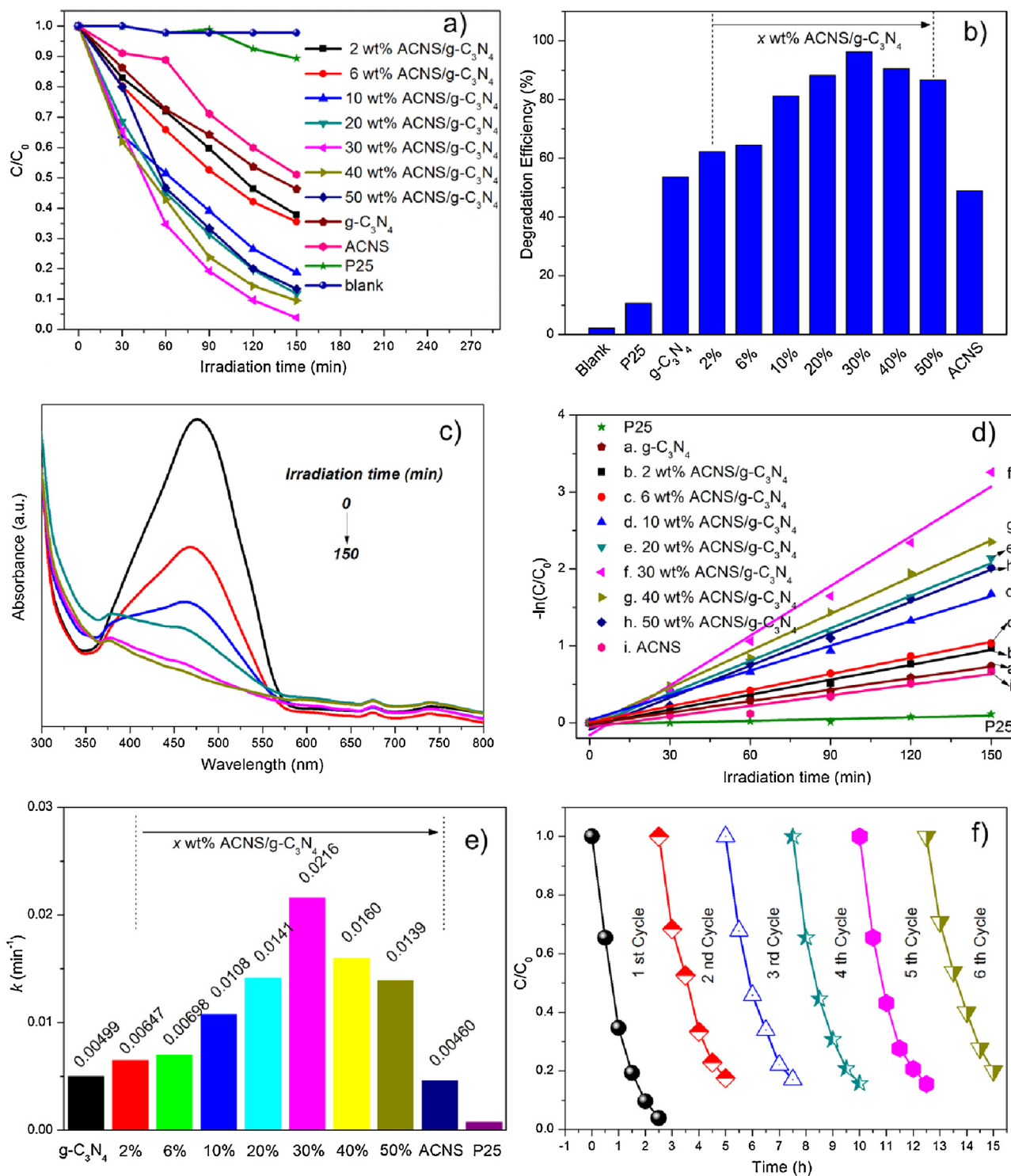**Fig. 9.** (a) Degradation rates and (b) efficiencies of MO by ACNS/g-C_3N_4 composite photocatalysts as a function of irradiation time. (c) The UV–vis spectra changes of MO as a function of irradiation time in the presence of 30 wt.% ACNS/g-C_3N_4 photocatalyst. (d) Kinetic linear simulation curves of MO photocatalytic degradation over the ACNS/g-C_3N_4 composite photocatalysts. (e) The comparison of apparent rate constant k as a function of ACNS content. (f) Cycling runs in the presence of 30 wt.% ACNS/g-C_3N_4 composite photocatalyst.

plots of $(\alpha h\nu)^{1/2}$ *vs* photon energy are 2.72 and 3.69 eV for g-C_3N_4 and ACNS, respectively, as shown in Fig. 7b. The band gaps calculated herein are consistent with the literature values [29,32,42].

The XPS measurements are carried out to investigate the chemical environment and surface stoichiometry of the elements of samples. The survey XPS spectra of g-C_3N_4 (Fig. 8a) reveal that the elements of C, O, and N exist on the surface of pristine g-C_3N_4, a weak O 1s peak at 532.1 eV is accredited to the adsorbed H_2O or CO_2, which is a common phenomenon found in literatures [43]. While the elements of C, O, N and Cl can be detected in ACNS, which indicates that chloride ions are indeed embedded in the g-C_3N_4 layers, its content is 0.7% (atom ratio) from XPS. The Cl elements is also found for the 30 wt.% ACNS/g-C_3N_4 sample besides C, O and N elements (Fig. 8b), which indicates that ACNS/g-C_3N_4 is
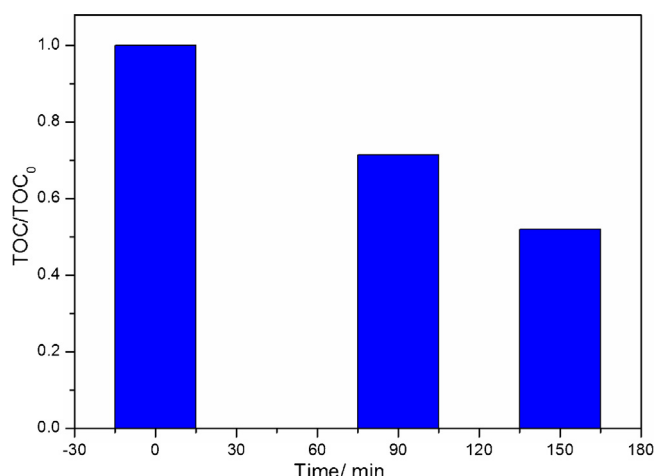
Fig. 10. TOC removal of MO over 30 wt.% ACNS/g-C$_3$N$_4$ composites under visible light illumination.

successfully developed by a sonication-assisted electrostatic self-assembly approach. The corresponding high resolution spectra of C1s, N1s, O1s and Cl 2p are also given for corresponding sample. The XPS spectra of the C 1s core level for g-C$_3$N$_4$ can be deconvoluted into two components including the standard reference carbon (284.8 eV) and the sp^2-bonded C in N=C(−N)$_2$ (288.3 eV) [8,22,32] (Fig. 8c). The N1s spectrum of g-C$_3$N$_4$ can be deconvoluted into four peaks (Fig. 8e). The main peak at 398.7 eV is assigned to sp^2 nitrogen (C=N−C) involved in triazine rings, while the peak at 399.8 eV originates from the tertiary nitrogen bonded to carbon atoms in the form of N–(C)$_3$ [13,32,44]. The peak at 401.3 eV is ascribed to amino functions (C−N−H). Another peak centered at 404.4 eV is associated to charging effects or positive charge localization in heterocycles [44]. These assignments of C1s and N1s agree well with the g-C$_3$N$_4$ reported previously. It is clear that, when forming the heterostructure, the N 1s feature peaks originated from amino functions (C−N−H) of g-C$_3$N$_4$ shift toward the lower binding energy side (401.1 eV), indicative of a strong chemical interaction between the two components of ACNS/g-C$_3$N$_4$ samples. Actually, when ACNS and g-C$_3$N$_4$ are close enough, Cl anion of ACNS possess a lone electron pair, resulting in bringing more negative charges to the amino functions (C−N−H) of tris-s-triazine unit of g-C$_3$N$_4$, which will form H-bonding and improve the electron density of amino functions (C−N−H), thus leading to an decrease in the binding energy (as shown in insert sketch in Fig. 9f). Moreover, it is even more evident when it comes to Cl 2p, typical characteristic doublet for chloride anions is observed at 2p$_{3/2}$(197.37 eV) and 2p$_{1/2}$ (198.85 eV) in Cl 2p of ACNS, which is referred to the typical characteristic of chloride anions [29,45]. The peak relating to the Cl 2p is shifted to the higher binding energy side 2p$_{3/2}$ (197. 73 eV) and 2p$_{1/2}$ (199.01 eV) for 30 wt.% ACNS/g-C$_3$N$_4$ compared with that of the ACNS, further indicating the possible bonding configuration of C−N−H−Cl$^{\ominus}$ formed between interface of two component in ACNS/g-C$_3$N$_4$ composite photocatalysts as we supposed above.

3.3. Photocatalytic properties of the ACNS/g-C$_3$N$_4$ photocatalysts

Before irradiation, the suspensions are magnetically stirred in dark for 30 min to get absorption-desorption equilibrium between the photocatalyst and dye molecular. It is obvious that the adsorption capacity of the ACNS/g-C$_3$N$_4$ increases with increasing ACNS contents compared with g-C$_3$N$_4$ (Fig. S1a), which may be attributed to the electrostatic attraction between the ACNS and MO molecules. The results are further exhibited directly by the adsorption percentage of different samples in Fig. S1b. The superior adsorption

capacity is in favor of improving photocatalytic activity because of the full contact between target molecules and photocatalyst [46].

The photocatalytic activity of ACNS/g-C$_3$N$_4$ composites are evaluated further under visible-light irradiation ($\lambda > 420$ nm). For comparison, the photocatalytic properties of P25, pristine g-C$_3$N$_4$ and ACNS are also tested under identical experimental conditions. The photodegradation process recorded by the temporal evolution of the spectra is shown in Fig. 9a, and the detailed degradation efficiency is presented as well in Fig. 9b. In the absence of photocatalyst, C/C$_0$ does not noticeably decay upon irradiation and therefore the degradation of MO is negligible, ruling out the direct photolysis of MO under visible-light irradiation. On the contrary, the photocatalytic performance is significantly enhanced in the presence of the ACNS/g-C$_3$N$_4$ photocatalysts, to be specific, the photocatalytic efficiency of g-C$_3$N$_4$ and ACNS for MO are 53.7% and 48.9% as shown in Fig. 9b, respectively. The ACNS shows no visible light absorption (Fig. 7a), while ACNS after adsorption with MO molecules shows obvious visible light adsorption (Fig. S3). Therefore, its photocatalytic activity under visible light irradiation seems possible attributed to dye-sensitized process, dye-sensitized phenomenon were reported always in TiO$_2$-based photocatalysts [47,48]. For the ACNS/g-C$_3$N$_4$ photocatalysts, it is obvious that the photocatalytic activity enhanced significantly with the increased amount of ACNS. When the ACNS amount is 30 wt.%, ACNS/g-C$_3$N$_4$ performs best and 96.2% MO is photo-degraded in 150 min. However, when the amount of ACNS is higher than 30 wt.%, the photocatalytic activity of the photocatalyst decreases gradually. Compared with the g-C$_3$N$_4$ and ACNS, the ACNS/g-C$_3$N$_4$ photocatalysts perform excellent photocatalytic activity. Fig. 9c illustrates the variations in MO absorbance around 476 nm using 30 wt.% ACNS/g-C$_3$N$_4$ photocatalyst. The absorbance obviously decreases with increased irradiation time. No absorbance peak is observed after irradiation for 2.5 h, which indicates MO's complete decomposition.

To quantitatively investigate the reaction kinetics of the MO degradation, the experimental data are fitted by applying a first-order model as expressed by Eq. (1). This equation is well established for photocatalytic experiments when the pollutant is within the millimolar concentration range [23],

$$-\ln\left(\frac{C}{C_0}\right) = kt \tag{1}$$

where C$_0$ and C are the dye concentrations in solution at times 0 and t, respectively, and k is the apparent first-order rate constant. Fig. 9d shows the effect of ACNS content on the MO photodegradation rate with ACNS/g-C$_3$N$_4$ photocatalysts. Upon varying the ACNS content, the plot of the irradiation time (t) against $-\ln(C/C_0)$ is nearly straight line. Fig. 9e shows that the ACNS content greatly influence the photo-degrading rate (k) of the composite samples. The ACNS content is pivotal for achieving the high photocatalytic activity of the ACNS/g-C$_3$N$_4$ composite. The 30 wt.% ACNS/g-C$_3$N$_4$ exhibits the highest photodegradation efficiency, which is about 4.3 and 5-folds higher than that of g-C$_3$N$_4$ and ACNS, respectively. The suitable ACNS content cause its well dispersion on the g-C$_3$N$_4$ surface, which favored the transfer and separation of the charge carriers. However, at contents higher than 30 wt.%, photocatalytic activity of the ACNS/g-C$_3$N$_4$ composites photocatalysts declined.

In order to determine the residual dye and intermediates of MO over 30 wt.% ACNS/g-C$_3$N$_4$, ESI/MS was used and Mass spectrum intensity variation of the fragment ions peaks appearing under different photoexcitation time was shown in Fig. S4. After irradiation, some fragment ions, such as $m/z = 261$ [C$_{12}$H$_9$N$_2$SO$_3$]$^-$, $m/z = 173$[C$_6$H$_5$SO$_4$]$^-$ and $m/z = 157$ [C$_6$H$_5$SO$_3$]$^-$, *etc.* emerges. Along with irradiation time retention, some degradation intermediate products decomposed gradually to smaller molecule fragment, the possible fragment ions of MO was displayed in Fig. S5. The total organic carbon (TOC) analysis was also used to assess
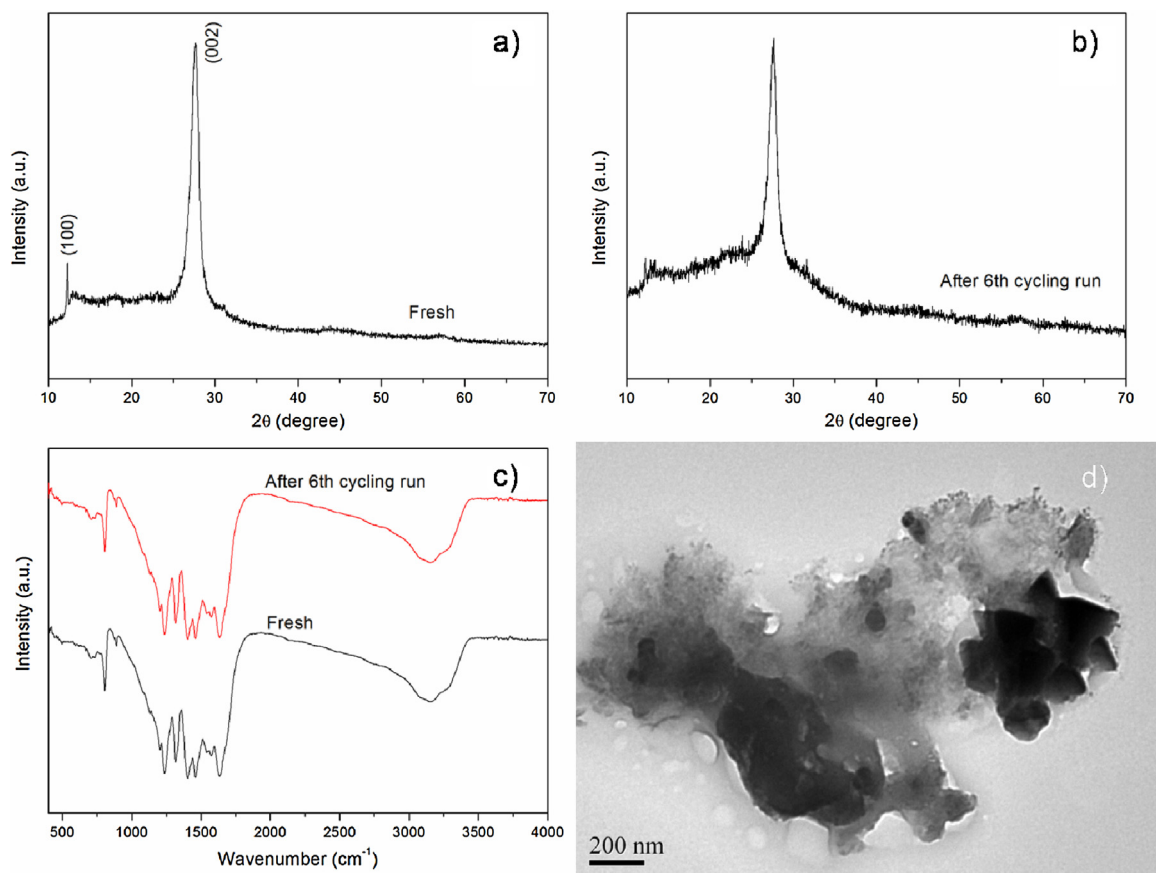
Fig. 11. (a, b) XRD patterns, (c) FTIR spectra, (d) TEM of 30 wt.% ACNS/g-C_3N_4 photocatalyst after 6 times cycling run.
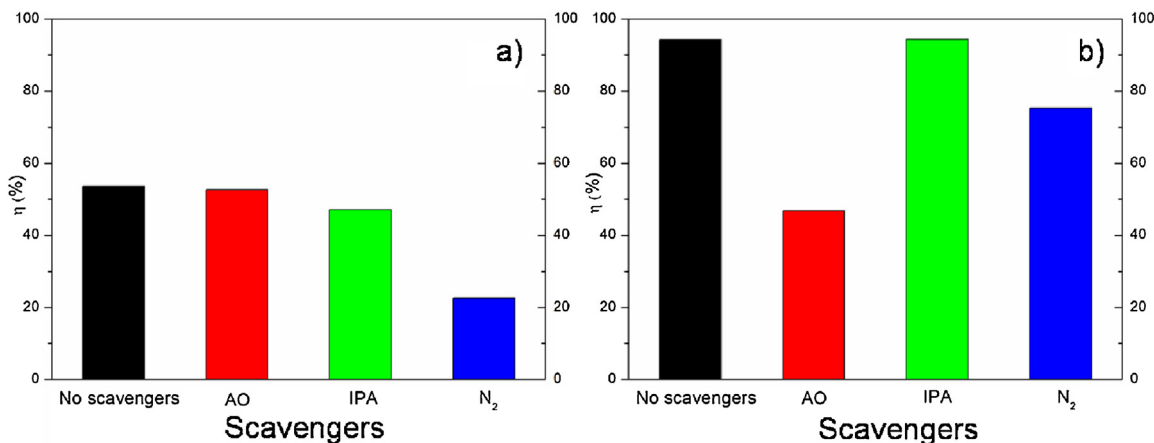

Fig. 12. Effect of a series of scavengers on the photocatalytic efficiencies of samples. (a) g-C_3N_4; (b) 30.0 wt.% ACNS/g-C_3N_4 photocatalyst. (The dosage of scavengers = 0.1 mmol L^{-1}, illumination time t = 150 min).

the mineralization ratio of MO in water over 30 wt.% ACNS/g-C_3N_4 under visible-light illumination. As illustrated in Fig. 10, the removal of TOC was about 48.1% after 150 min reaction. It is meant after photodegradation, about 48.1% organic carbon over MO is transformed into inorganic carbon (CO_2). It is verified that MO is indeed photocatalytic degraded by the composite, rather than just decolorized by the light irradiation.

The stability of a photocatalyst is important for its assessment and application. The stability and reusability of 30 wt.% ACNS/g-C_3N_4 heterostructure is tested under identical reaction conditions. After the complete degradation of MO dye, the catalyst is collected by centrifugation, washed with deionized water several times,

dried in an oven at 60 °C for 12 h and then used for the next run. As shown in Fig. 9f, degradation efficiency decline to 83% in the second cycle and no significant drop is found for the following cycle run. The hybrid photocatalyst is found to be reusable and considerable photoactivity is achieved after the sixth run. And the removal efficiency is maintained at around 85% in the 6th recycling test. We suppose that the mass loss of ACNS in the progress of collection is the one of reasons for the decrease in photocatalytic activity of reused photocatalyst in repeated cycles. More importantly, physical adsorptions of dye molecular over the surface of composites photocatalysts keep reactive molecular away from the active sites during the cycling run [49]. The XRD analysis before and after the

6 times photocatalytic reaction is present in Fig. 11a, b. Careful observation further shows the decline of the diffraction peak intensity at 12.25, indicating that the adsorption of MO molecules with the layers of ACNS. It may be the main reason for the decline of photocatalytic activity for the second run. Nevertheless, superior photo-degradation efficiency after 6th run was preserved. In addition, the FTIR spectra of the 30 wt.% ACNS/g-C_3N_4 photocatalyst after 6 times tests remained almost unchanged compared with that of the fresh one (Fig. 11c), further indicating that the high stability of the ACNS/g-C_3N_4 under reaction condition. No significant aggregate is observed from TEM images for the 30 wt.% ACNS/g-C_3N_4 after 6 cycles as shown in Fig. 11d.

3.4. Proposed reaction mechanism of the ACNS/g-C_3N_4 photocatalysts

3.4.1. Determination of the reactive species

It has been reported that the $^\bullet O_2^-$, h^+, and $^\bullet OH$ are the major reactive species for the photocatalytic oxidation. In order to investigate the photocatalytic mechanism of the ACNS/g-C_3N_4 photocatalysts, several scavengers are used to explore the reactive species in the process of photocatalytic reaction. Adding different scavengers into reaction solutions to remove the corresponding reactive species, therefore the functions of the corresponding reactive species in the photocatalytic process based on the change of photocatalytic efficiency could be made clear. It is reported that the ammonium oxalate (AO) can be used to remove hole (h^+), and isopropanol (IPA) is employed to impair the hydroxyl radical ($^\bullet OH$), while the N_2 purging is applied to reduce the superoxide radical ($^\bullet O_2^-$) [21,34]. The results are shown in Fig. 12.

Fig. 12a shows the photocatalytic efficiency of MO, using g-C_3N_4 as photocatalyst with various scavengers. It is known that the photocatalytic efficiency of MO is 53.7% without scavengers. When the AO is added into reaction solution, the photocatalytic efficiency is almost invariable (52.6%). Therefore, holes are not the major reactive species. However, after the addition of IPA into reaction solution, the degradation efficiency of MO decreases to 47.1%. Finally, when N_2 is bubbled into reaction solution, the photocatalytic efficiency is whittled down into 22.6%. Based on the results, it is clear that both $^\bullet O_2^-$ and $^\bullet OH$ are the major reactive species in the photocatalytic reaction system for pristine g-C_3N_4 photocatalyst. The influencing degree is as follows, $^\bullet O_2^- > {}^\bullet OH > h^+$, which agrees well with the previous reports [11,34].

It is clear that in Fig. 12b the degradation efficiency of MO for the 30.0 wt.% ACNS/g-C_3N_4 photocatalyst is 96.2% without scavenger. When adding IPA into reaction solution, the photocatalytic efficiency is barely changed. However, after the addition of AO and purging of N_2 into the reaction system respectively, the degradation efficiency of MO is whittled down into 46.8% and 75.3%, respectively. Obviously, h^+ and $^\bullet O_2^-$ are the major reactive species for the 30.0 wt.% ACNS/g-C_3N_4 photocatalyst. The influencing degree is as follows, $h^+ > {}^\bullet O_2^- > {}^\bullet OH$.

3.4.2. Photoluminescence (PL) emission spectra

The PL emission spectra is employed to investigate the combination and separation of the photoinduced carriers which play a crucial role in photocatalytic reactions. The intensity of PL emission spectra indicates the recombination speed of photoexcited electron-hole pairs. The stronger the PL intensity is, the faster the combination of the photoexcited electron-hole is [34]. Generally, a higher PL intensity indicates a higher recombination rate of photoexcited electron-hole carriers, while a lower PL intensity expresses a lower recombination rate of photoexcited electron-hole carriers [34,41]. Fig. 13 shows the PL spectra of the ACNS/g-C_3N_4 photocatalysts with wt.% of 10.0, 20.0, 30.0, 50.0 and g-C_3N_4, respectively. It is clear that the PL spectra of the photocat-
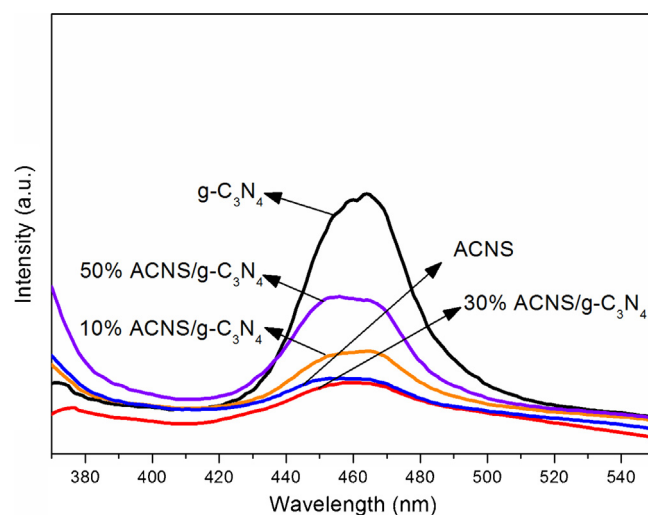
Fig. 13. Photoluminescence (PL) spectra of ACNS/g-C_3N_4 photocatalysts.
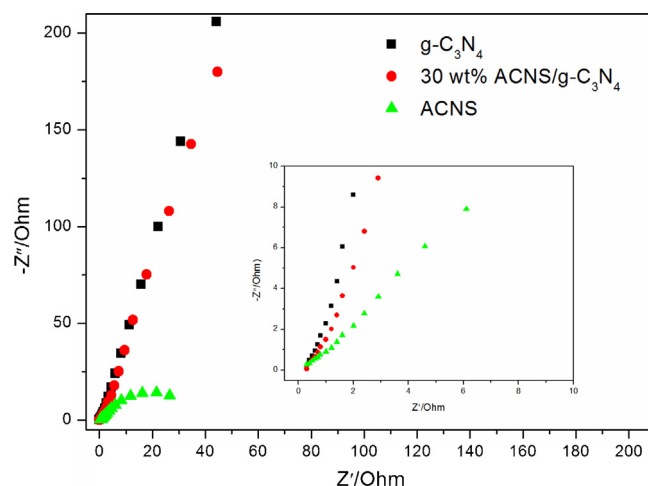
Fig. 14. EIS Nyquist plots of the g-C_3N_4, ACNS and ACNS/g-C_3N_4 photocatalysts under the irradiation of visible light. All the electrodes were evaluated in 0.1 M Na_2SO_4 aqueous solution.

alysts have a strong emission peak at around 460 nm, which could be related to the recombination of the photoexcited electrons and holes of g-C_3N_4 [21,23,34]. The position of the ACNS/g-C_3N_4 emission peaks is similar with that of g-C_3N_4. The emission intensity of the ACNS/g-C_3N_4 composite photocatalysts significantly decreases, especially with the 30 wt.% ACNS/g-C_3N_4 sample having the weakest intensity among ACNS/g-C_3N_4 samples. These results clearly indicate that the recombination of photo-generated charge carriers is inhibited in the composite semiconductors. The above results are consistent well with the results of photocatalytic activity of the ACNS/g-C_3N_4 photocatalysts.

3.4.3. Electrochemical properties of ACNS/g-C_3N_4 composite photocatalysts

Furthermore, electrochemical impedance spectroscopy (EIS) is used to investigate the photogenerated charge separation process. EIS Nyquist plots of g-C_3N_4, ACNS and 30.0 wt.% ACNS/g-C_3N_4 electrodes under visible light irradiation are shown in Fig. 14. A smaller arc radius of the EIS Nyquist plot suggests an effective separation of photogenerated electron-hole pairs and fast interfacial charge transfer [11,29,45]. The arc radius on EIS Nyquist plot of ACNS/g-C_3N_4 heterojunction is smaller than that of g-C_3N_4. These results indicate the dramatically enhanced separation and trans-
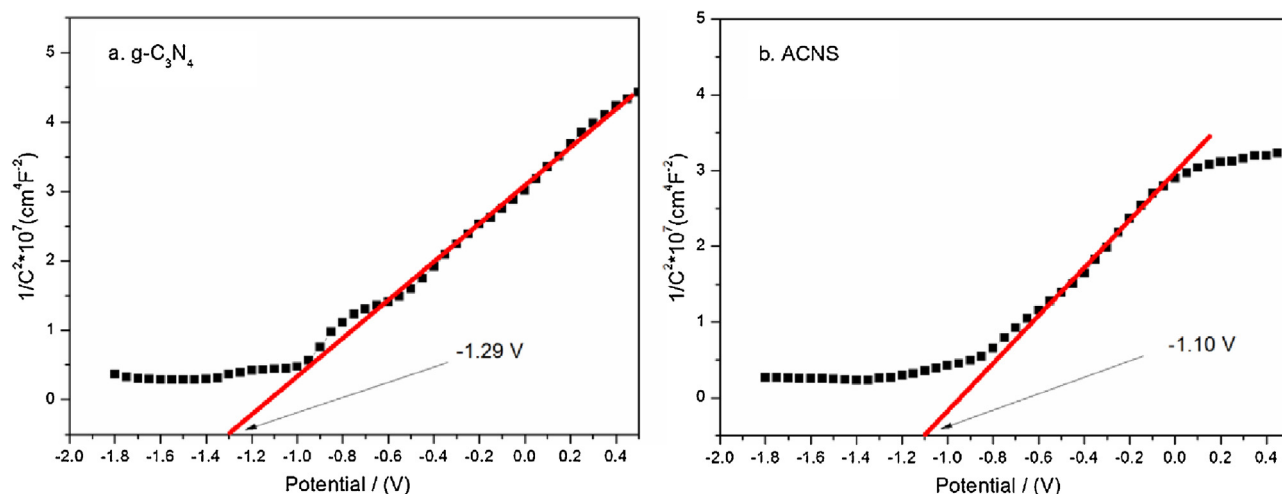
Fig. 15. Mott–Schottky plots collected for (a) g-C_3N_4 and (b) ACNS at a frequency of 1000 Hz in the dark.
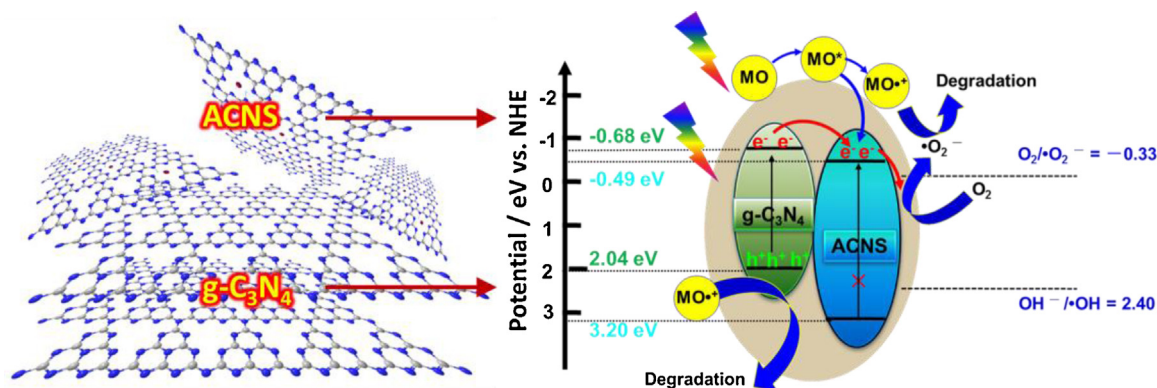

Fig. 16. Schematic illustration of electron-hole separation and transport in the g-C_3N_4/ACNS heterostructured photocatalyst.

fer efficiency of electron-hole pairs in ACNS/g-C_3N_4 composites photocatalysts.

The Mott–Schottky method was employed to determine the electronic potentials of g-C_3N_4 and ACNS. As we know, different semiconductor materials have different Fermi level potentials. When a composite is formed by two different semiconductor materials, a new balance of the Fermi level will eventually reach due to the opposite movement of the Fermi levels of these two semiconductors. With the shift of the Fermi level, electrons and holes will exchange on the interface between them and an interfacial electric field will be built [50]. Fig. 15 shows the Mott–Schottky plots of g-C_3N_4 and the ACNS thin-film photoelectrodes in 0.1 M Na_2SO_4 under dark condition. The flat band potential of a semiconductor material can be determined by extrapolating to $C^{-2} = 0$. The flat band potential of g-C_3N_4 was approximately −1.29 V (vs. Ag/AgCl) (Fig. 15), while that of the ACNS positively shifts to −1.10 V. The measured potentials can be converted to the reversible hydrogen electrode (RHE) scale via the Nernst equation [51]:

$$E_{RHE} = E_{Ag/AgCl} + 0.05916\,pH + E°_{Ag/AgCl} \qquad (2)$$

where E_{RHE} is the converted potential vs RHE, $E_{Ag/AgCl}$ is the experimental potential measured against the Ag/AgCl reference electrode, and $E°_{Ag/AgCl}$ is the standard potential of Ag/AgCl at 298 K (0.1976 V). The calculated conduction band edges of g-C_3N_4 and ACNS are −0.68 eV and −0.49 eV, respectively. The difference in their flat-band potential demonstrates that a heterojunction electric field was formed on the interface between g-C_3N_4 and ACNS. In addition, the existence of this electric field significantly increases the

separation efficiency of the photogenerated electrons and holes and therefore dramatically enhances the photocatalytic degradation performance of the ACNS/g-C_3N_4 composite.

3.4.4. Proposed mechanism of the ACNS/g-C_3N_4 photocatalyst

According to the above information, the CB potential of ACNS is shown to be more positive than that of g-C_3N_4. With the band gap energies shown in Fig. 7, the VB position of g-C_3N_4 and ACNS are calculated to be 2.04 and 3.20 eV, indicating that the VB potential of ACNS is more positive than that of g-C_3N_4. On the basis of VB and CB levels of g-C_3N_4 and ACNS, the reactive species of ACNS/g-C_3N_4 reaction systems together with PL emission spectra results, a band structure diagram for ACNS/g-C_3N_4 phase heterostructure can be drawn as shown in Fig. 16. For ACNS solely, MO molecules adsorbed on the ACNS surface produces self-photosensitized reaction, the generated electron from the excited MO molecules are injected into the CB of ACNS, it is reported the redox potential of $O_2/•O^{2-}$ is −0.33 eV vs NHE [52], which is more positive than conduction band potential of ACNS (-0.49 eV vs NHE). Thus the cation radical of MO could be efficiently degraded with the aid of high oxidizing-power of the $•O^{2-}$. Upon visible-light irradiation of ACNS/g-C_3N_4 heterostructure, the ACNS itself can be seldomly excited under visible light irradiation. While g-C_3N_4 absorbs the visible light, it can induce π-π^* transition and transport the excited-state electrons from the VB to the CB [20,21,23]. Since the CB position of g-C_3N_4 is higher than the CB position of ACNS, the photogenerated electrons tend to transfer from g-C_3N_4 to ACNS driven by offset of 0.19 eV, making charge separation more efficient and reducing the proba-

bility of recombination. Thus, the electrons in the CB of ACNS would subsequently transfer to the surface of photocatalyst to react with surface chemisorbed oxygen to yield superoxide radicals $\cdot O_2^-$ ($E(O_2/\cdot O_2^-)$ = −0.33 eV vs. NHE), then $\cdot O_2^-$ may also react with H^+ to further produce hydroxyl radicals $\cdot OH$ [19,34]. Both $\cdot O_2^-$ and $\cdot OH$ all can oxidize dye molecular due to their high oxidative capacity [11,23,41], at the same time, the holes from g-C_3N_4 can also directly oxidize dye molecular. Therefore, as mentioned above, the facilitated charge transfer in ACNS/g-C_3N_4 composites photocatalysts effectively reduces the recombination of photoinduced electrons and holes, resulting in enhanced photodegradation efficiency under the visible light irradiation.

4. Conclusion

In conclusion, the visible-light-induced ACNS/g-C_3N_4 isotype heterojunction photocatalysts are synthesized by introducing acidified g-C_3N_4 via a sonication-assisted electrostatic self-assembly approaches. In photocatalytic reaction system, the photogenerated electrons tend to transfer from the CB of g-C_3N_4 to that of ACNS, resulting in efficient charge separation and thus reduce the probability of recombination. The electrons in the CB of ACNS exhibit high reducibility to reduce the molecular oxygen to yield $\cdot O_2^-$, and the holes in the VB of g-C_3N_4 display high oxidizability in oxidizing dye molecular. Therefore, this kind of novel isotype heterojunction with promoted charge separation shows significant enhancement in the photocatalytic activity for MO degradation under visible light irradiation. The isotype heterostructure strategy here developed could provide new perspectives for sustainable utilization of solar irradiation and constructing other functionalized g-C_3N_4 heterostructure to promote charge separation for high performance photocatalysts. Furthermore, promising functionalized g-C_3N_4 could be facilely prepared by counteranion exchange by aid of protonation. Thus, functionalized g-C_3N_4-based heterojunctions can also be envisaged in solar energy conversion, photosynthesis, photovoltaic devices, and so on.

Competing interest

The authors declare no competing financial interest.

Acknowledgments

Appendix A. Supplementary data

Supplementary data associated with this article can be found, in the online version, at http://dx.doi.org/10.1016/j.apcatb.2016.03.060.

References

[1] K.S. Liu, M.Y. Cao, A. Fujishima, L. Jiang, Chem. Rev. 114 (2014) 10044–10094.
[2] A. Fujishima, T.N. Rao, D.A. Tryk, J. Photochem. Photobiol. C 1 (2000) 1–21.
[3] K. Ma, O. Yehezkeli, D.W. Domaille, H.H. Funke, J.N. Cha, Angew. Chem. Int. Ed. 54 (2015) 11490–11494.
[4] R. Pol, M. Guerrero, E. García-Lecina, A. Altube, E. Rossinyol, S. Garroni, M.D. Baró, J. Pons, J. Sort, E. Pellicer, Appl. Catal. B: Environ. 181 (2016) 270–278.
[5] C.Y. Teh, T.Y. Wu, J.C. Juan, Catal. Today 256 (2015) 365–374.
[6] J.J. Zhu, P. Xiao, H.L. Li, S.A.C. Carabineiro, ACS Appl. Mater. Interfaces 6 (2014) 16449–16465.
[7] Y. Zheng, J. Liu, J. Liang, M. Jaroniec, S.Z. Qiao, Energy Environ. Sci. 5 (2012) 6717–6731.
[8] X.C. Wang, K. Maeda, A. Thomas, K. Takanabe, G. Xin, J.M. Carlsson, K. Domen, M. Antonietti, Nat. Mater. 8 (2008) 76–80.
[9] Z.W. Zhao, Y.J. Sun, F. Dong, Nanoscale 7 (2015) 15–37.
[10] S.C. Yan, Z.S. Li, Z.G. Zou, Langmuir 25 (2009) 10397–10401.
[11] X.J. Bai, L. Wang, Y.J. Wang, W.Q. Yao, Y.F. Zhu, Appl. Catal. B: Environ. 152–153 (2014) 262–270.
[12] Y.D. Hou, Y.S. Zhu, Y. Xu, X.C. Wang, Appl. Catal. B: Environ. 156–157 (2014) 122–127.
[13] J. Ding, Q.Q. Liu, Z.Y. Zhang, X. Liu, J.Q. Zhao, S.B. Cheng, B.N. Zong, W.L. Dai, Appl. Catal. B: Environ. 165 (2015) 511–518.
[14] C.S. Xing, Z.D. Wu, D.L. Jiang, M. Chen, J. Colloid Interface Sci. 433 (2014) 9–15.
[15] P. Niu, L.L. Zhang, G. Liu, H.M. Cheng, Adv. Funct. Mater. 22 (2012) 4763–4770.
[16] Q.H. Liang, Z. Li, X.L. Yu, Z.H. Huang, F.Y. Kang, Q.H. Yang, Adv. Mater. 27 (2015) 4634–4639.
[17] J.S. Zhang, M.W. Zhang, R.Q. Sun, X.C. Wang, Angew. Chem. Int. Ed. 51 (2012) 10145–10149.
[18] Z.Y. Zhang, J.D. Huang, M.Y. Zhang, Q. Yuan, B. Dong, Appl. Catal. B: Environ. 163 (2015) 298–305.
[19] H.P. Li, J.Y. Liu, W.G. Hou, N. Du, R.J. Zhang, X.T. Tao, Appl. Catal. B: Environ. 160–161 (2014) 89–97.
[20] Y. Hou, Z.H. Wen, S.M. Cui, X.R. Guo, J.H. Chen, Adv. Mater. 25 (2013) 6291–6297.
[21] K. Li, S.M. Gao, Q.Y. Wang, H. Xu, Z.Y. Wang, B.B. Huang, Y. Dai, J. Lu, ACS Appl. Mater. Interfaces 7 (2015) 9023–9030.
[22] W.K. Jo, T.S. Natarajan, Chem. Eng. J. 281 (2015) 549–565.
[23] L. Ge, C.C. Han, J. Liu, Appl. Catal. B: Environ. 108–109 (2011) 100–107.
[24] Z.C. Yang, J. Li, F.X. Cheng, Z. Chen, X.P. Dong, J. Alloy Compd. 634 (2015) 215–222.
[25] Y.J. Sun, W.D. Zhang, T. Xiong, Z.W. Zhao, F. Dong, R.Q. Wang, W.K. Ho, J. Colloid Interface Sci. 418 (2014) 317–323.
[26] F. Dong, Z.W. Zhao, T. Xiong, Z.L. Ni, W.D. Zhang, Y.J. Sun, Wing-Kei Ho, ACS Appl. Mater. Interfaces 5 (2013) 11392–11401.
[27] Y.J. Zhang, A. Thomas, M. Antonietti, X.C. Wang, J. Am. Chem. Soc. 131 (2008) 50–51.
[28] T.Y. Ma, Y.H. Tang, S. Dai, S.Z. Qiao, Small 10 (2014) 2382–2389.
[29] X.R. Du, G.J. Zou, Z.H. Wang, X.L. Wang, Nanoscale 7 (2015) 8701–8706.
[30] X.D. Zhang, X. Xie, H. Wang, J.J. Zhang, B.C. Pan, Y. Xie, J. Am. Chem. Soc. 135 (2013) 18–21.
[31] W.J. Ong, L.L. Tan, S.P. Chai, S.T. Yong, A.R. Mohamed, Nano Energy 13 (2015) 757–770.
[32] G.S. Wu, S.S. Thind, J.L. Wen, K. Yan, A.C. Chen, Appl. Catal. B: Environ. 142–143 (2013) 590–597.
[33] M. Groenewolt, M. Antonietti, Adv. Mater. 17 (2005) 1789–1792.
[34] S.F. Chen, Y.F. Hu, S.G. Meng, X.L. Fu, Appl. Catal. B: Environ. 150–151 (2014) 564–573.
[35] Y.P. Zhu, T.Z. Ren, Z.Y. Yuan, ACS Appl. Mater. Interfaces 7 (2015) 16850–16856.
[36] S.W. Zhang, J.X. Li, X.K. Wang, Y.S. Huang, M.Y. Zeng, J.Z. Xu, J. Mater. Chem. A 3 (2015) 10119–10126.
[37] M. Tahir, C.B. Cao, N. Mahmood, F.K. Butt, A. Mahmood, F. Idrees, S. Hussain, M. Tanveer, Z. Ali, I. Aslam, ACS Appl. Mater. Interfaces 6 (2014) 1258–1265.
[38] Y. Feng, J.C. Shen, Q.F. Cai, H. Yang, Q.H. Shen, N. J. Chem. 39 (2015) 1132–1138.
[39] B. Balamurugan, I. Aruna, B.R. Mehta, S.M. Shivaprasad, Phys. Rev. B 69 (2004) 1654191–1654195.
[40] N. Sakai, Y. Ebina, K. Takada, T. Sasaki, J. Am. Chem. Soc. 126 (2004) 5851–5858.
[41] K. Dai, L.H. Lu, C.H. Liang, Q. Liu, G.P. Zhu, Appl. Catal. B: Environ. 156–157 (2014) 331–340.
[42] G.G. Zhang, M.W. Zhang, X.X. Ye, X.Q. Qiu, S. Lin, X.C. Wang, Adv. Mater. 26 (2014) 805–809.
[43] F. Jiang, T.T. Yan, H. Chen, A.W. Sun, C.M. Xu, X. Wang, Appl. Surf. Sci. 295 (2014) 164–172.
[44] D.Q. Gao, Q. Xu, J. Zhang, Z.L. Yang, M.S. Si, Z.J. Yan, D.S. Xue, Nanoscale 6 (2014) 2577–2581.
[45] X.F. Chang, S.B. Wang, Q. Qi, M.A. Gondal, S.G. Rashid, D.Y. Yang, M.A. Dastageer, K. Shen, Q.Y. Xu, P. Wang, Appl. Catal. B: Environ. 176–177 (2015) 201–211.
[46] Q. Liu, Y.R. Guo, Z.H. Chen, Z.G. Zhang, X.M. Fang, Appl. Catal. B: Environ. 183 (2016) 231–241.
[47] H. Kyung, J. Lee, W. Choi, Environ. Sci. Technol. 39 (2005) 2376–2382.
[48] J.C. Zhao, T.X. Wu, K.Q. Wu, K. Oikawa, H. Hidaka, N. Serpone, Environ. Sci. Technol. 32 (1998) 2394–2400.
[49] S. Shi, M.A. Gondal, A.A. Al-Saadi, R. Fajgar, J. Kupcik, X.F. Chang, K. Shen, Q.Y. Xu, Z.S. Seddigi, J. Colloid Interface Sci. 416 (2014) 212–219.
[50] Y.Y. Bu, Z.Y. Chen, C. Feng, W.B. Li, RSC Adv. 4 (2014) 38124–38132.
[51] M.L. Li, L.X. Zhang, X.Q. Fan, Y.J. Zhou, M.Y. Wu, J.L. Shi, J. Mater. Chem. A 3 (2015) 5189–5196.
[52] G.J. Xing, C.H. Tang, B. Zhang, L.X. Zhao, Y.G. Su, X.J. Wang, J. Alloy Compd. 647 (2015) 287–294.